

CLOUDY and the High-Resolution Microcalorimeter Revolution: Optical, UV, and X-ray Spectra of One-electron Systems

CHAMANI M. GUNASEKERA ¹, PETER A. M. VAN HOOF ², MARIOS CHATZIKOS ³ AND GARY J. FERLAND ³

¹*Space Telescope Science Institute
3700 San Martin Drive, Baltimore, MD 21218*

²*Royal Observatory of Belgium
Ringlaan 3, 1180 Brussels, Belgium*

³*Department of Physics & Astronomy, University of Kentucky
Lexington, KY 40506, USA*

ABSTRACT

The majority of the baryonic matter in the universe is in the form of astrophysical plasmas. The mass of the hot X-ray emitting gas in a cluster of galaxies has more mass than the galaxies in the cluster. With the launch of the XRISM microcalorimeter mission, space-based X-ray observations will achieve a record spectral resolving power of $R \equiv E/\Delta E \sim 1200$. With this resolving power, emission features associated with fine-structure energy levels of some species will be resolved, sometimes for the first time. The plasma code, CLOUDY, was not originally designed for high-resolution X-ray spectroscopy and throughout its history did not resolve fine-structure components of Lyman lines. Here we expand CLOUDY to resolve these fine-structure energy levels and obtain predicted X-ray spectra that match the resolution of new microcalorimeter observations. We show how the Lyman lines can be used as column density indicators and examine their sensitivity to external radiation fields and turbulence.

Keywords: X-ray binary stars – atomic data – radiative transfer

1. INTRODUCTION

There are a multitude of astrophysical objects that emit X-rays, from galaxy clusters to supernova remnants to X-ray binaries and many more. X-ray astronomy has developed into an extensive field of research, and has made significant strides in understanding the hot and energetic universe. X-ray emission is mainly produced in gas at temperatures from 10^6 to 10^8 K, with most detectors working in the 0.1 to 10 keV range (XRISM Science Team 2020).

CLOUDY conducts simulations of non-equilibrium plasmas and predicts the entire spectrum including X-ray line intensities. In early CLOUDY versions, the emphasis was on producing high-resolution optical, UV and IR spectra, with the X-ray region treated to the precision only required by the then-existing missions (Ferland et al. 1998). Microcalorimeters allow unprecedented resolution in the X-ray regime, so CLOUDY must be improved to match this. This work is part of an effort to improve CLOUDY for work in X-ray astronomy

(PI: Chatzikos). Specifically, it aims to resolve the Lyman¹ lines into its fine-structure components, which are observable features in microcalorimeter data.

A series of updates to CLOUDY were made, aimed to prepare the code for modelling microcalorimeter spectra. CLOUDY treats 1 and 2 electron systems with a unified approach along iso-sequences. We expanded the two-electron iso-sequence with optical emission lines in mind (Porter et al. 2012, 2013). Subsequently we extended the CLOUDY framework on line formation processes for two-electron species that improved upon the accuracy of level energies and line wavelengths to meet the spectral resolution of X-ray microcalorimeter missions (Chakraborty et al. 2020a,b, 2021, 2022). For many-electron systems, CLOUDY uses atomic databases (Lykins et al. 2015), and Gunasekera et al. (2022) updated the CHIANTI atomic database, improving the calculated line wavelengths and intensities. The upcoming 2025 release of CLOUDY (C25) will

¹The Siegbahn notation in X-ray spectroscopy is typically used for inner-shell transitions, while the Lyman series in atomic physics is reserved for hydrogen-like ions. In this paper, we will use the latter notation, following the standard practice in X-ray astronomy. So for instance, we will notate the spectroscopic lines arising from the L shell ($2p$) \rightarrow K shell ($1s$) for H-like ions as Ly α .

further update Chianti to 10.1 (Dere et al. 2023). Many codes, CLOUDY included, rely upon the Kaastra & Mewe (1993) database of X-ray transitions, which does not have sufficiently accurate wavelengths for present-day microcalorimeters. To make their widely used data files even more valuable, we are taking the approach of producing patch files to update their energies (Camilloni et al. 2021) to current standards.

The np subshell of H-like ions is split into two fine-structure levels (with $j = 1/2, 3/2$) by the spin-orbit interaction between an atomic nucleus and the atomic electron (Bethe & Salpeter 1957). In many spectroscopic observations, the $np \rightarrow 1s$ transitions appear as single lines. For instance, lines like H I Ly α are actually doublets although to the best of our knowledge they have never been resolved in astrophysical spectra. As a result, versions of CLOUDY up to now have not resolved one-electron doublets. As we show below, the doublet spacing increases as nuclear charge (Z) increases, and iron-peak elements display two lines that are well separated in microcalorimeter observations. This work expands CLOUDY to predict such transitions, by improving the treatment of one-electron systems in order to match the resolving power of the new X-ray missions.

This paper is organized along the steps we took to resolve the one-electron doublets. In Section 2, first we outline a strategy that leverages our existing infrastructure, which applies over a broad range of physical conditions and obeys thermodynamic limits under the appropriate conditions. Then in Section 3 we detail the atomic structure and rates needed to simulate X-ray spectra. Section 4 discusses several unique radiative transfer issues that arise along the one electron sequence. We show spectra in some simple cases for a simulation of the Hitomi spectrum of the Perseus cluster.

2. ONE-ELECTRON DOUBLETS IN CLOUDY

2.1. CLOUDY's Previous Strategy

CLOUDY has long treated one and two-electron systems with great care for several reasons. The first is due to the large abundance of hydrogen and helium which, together, make up 99.9% of the atoms in the universe. The second distinction is that the energy-level structures of one and two-electron systems are quite different from the complex energy structure that is found in many-electron systems like, for instance, O II and O III. As shown in Figure 3 of Ferland et al. (2013), the first excited state of one and two electron systems is at roughly 3/4 of the ionization potential, and most of the states are very close to the continuum above. These highly excited levels called the Rydberg states in atomic physics, mediate the recombination process, affecting the ionization. Hydrogen and helium, in particular, must be treated with great care because they determine the ionization structure of a cloud (Chapter 2 of Osterbrock & Ferland (2006) and their recombination lines are important in determining the composition and ionization

of clouds across the universe (Chapter 5 of Osterbrock & Ferland (2006)).

The Rydberg levels pose several interesting problems. An infinite number exists in the low-density limit, although the number of levels is truncated at finite densities due to continuum lowering (Alimohamadi & Ferland 2022). We must sum over all the levels to obtain the total recombination coefficient and predict the ionization correctly. The higher levels collisionally couple to the continuum to bring the atom's ionization into LTE or STE at high particle or photon densities. So, again, many levels must be included. Many strong optical and infrared lines have upper levels in the Rydberg states, so we must determine their level populations with some precision to predict the spectrum. The fundamental problem is to treat a very large number of levels with the available computer hardware.

Our treatment of the Rydberg levels has changed as computers have become faster. Initially, we used several pseudo-states to represent the closely-spaced Rydberg levels at high principal quantum numbers (Cota 1987; Ferguson & Ferland 1997). The pseudo-states allowed the atom to go to LTE and STE limits when the particle or photon densities were sufficiently high (Ferland & Rees 1988; Ferland & Persson 1989). A disadvantage to this approach was that the pseudo-states affected the accuracy of the H and He recombination-line intensities. This approach reproduced classical Case B Osterbrock & Ferland (2006) intensities of H and He recombination lines to better than five percent.

Recombination lines must be predicted to high precision for certain applications, such as the primordial helium abundance of the universe, (Ferland et al. 2010) or for denser environments, where collisional and radiative transfer effects may be important (Ferland 1999a). Classical case B productions do not describe such clouds, so detailed radiative transfer must be done simultaneously with the solution of the emission and ionization.

As computers became faster, it became possible to remove the pseudo-states and replace them with models of higher- n shells. This advance was described in a series of papers that focused on measurements of the primordial helium abundance (Bauman et al. 2005; Porter et al. 2005, 2007, 2009, 2012). Ferland et al. (2013) is the culmination of this development. Figure 1 of that paper shows our model for one-electron systems. We use nl -resolved states for low principal quantum numbers. ‘‘Collapsed states’’, which are not l -resolved, were used for high n where l -changing collisions should bring the nl populations into $g = 2l + 1$ statistical equilibrium.

Pseudo-states are no longer used to describe the recombination and line-producing physics in our current approach. Beginning with C13, we use a finite number of collapsed and resolved levels, with a small amount of ‘‘top off’’ recombination coefficient being added to the highest level to reproduce

the total recombination to all levels. This approach had a problem near photoionization edges such as the Lyman jump. This is shown in figures 7 and 8 of [Ferland et al. \(2017\)](#). In nature, the very high- n Lyman lines merge onto the Lyman continuum above the bound levels, and no discontinuous Lyman jump is present ([Born 1969](#); [Ferland et al. 2017](#), Section 3.1.4). A finite model produces gaps in the spectrum just longward of the ionization edge where unmodelled high- n lines should add opacity. The continuum can “leak” through the cloud, as shown in Figure 8 of that paper. We dealt with this by adding many “extra” Lyman lines. These added opacity to the cloud but, in the original treatment, did not produce emission. The extra Lyman lines were sources of absorption opacity, so their upper-level population need not be known and they were not included in our level-population solver.

As outlined above, the original treatment of one-electron systems focused on light species such as H I or He II. We treat one and two electrons systems with a unified model that extends to the heaviest element treated, currently zinc ($Z = 30$). This is coded in such a way that it could be extended to very heavy elements if sufficient atomic data were available.

The following paragraph provides a brief overview, while subsequent sections will dive into greater detail. As described in the Introduction, high-resolution X-ray spectroscopy is becoming commonplace. The Lyman lines in one-electron systems are doublets. The discussion in the next section shows that the doublet separation is small for light elements, such as hydrogen and helium, and would not be resolvable for typical astrophysical kinetic temperatures ($\sim 10^4$ K). Previous developments had resolved nl but not the j -levels that introduce the doublet splitting. The doublet separation increases with the nuclear charge Z . Microcalorimeter X-ray missions will resolve the $\text{Ly}\alpha_{1,2}$ doublets for elements heavier than calcium ([Gunasekera et al., A&A, submitted](#)). The doublet separation depends on n . It is largest for the 2-1 transition and decreases as n increases. Future X-ray missions will resolve lower- n transitions of higher- Z species. CLOUDY has long treated up to zinc. However, this treatment can be extended to any Z and any principle quantum number n that the user specifies. Thus, the present development will be able to contribute greatly to multi-messenger studies, where emission from high- Z elements, such as gold, are of importance.

This paper will further develop the extra Lyman lines described in [Ferland et al. \(2017\)](#) to predict doublet emission. We use the existing level and ionization population solvers, which are nl but not j resolved, to determine the populations of upper (2P_j) levels and include the emission that results. We show synthetic spectra of Hitomi’s observations of the Perseus cluster.

2.2. Overview of the New Strategy

We adopted a strategy to resolve the Lyman doublets within the pre-existing framework. In Section 3, we describe each step in greater detail.

Extensive tests show that the existing one-electron populations solvers go to all thermodynamic limits. This includes LTE at high densities, STE when exposed to a true blackbody, the highly ionized Compton limit, and the fully molecular limit where most H is in the form of H_2 . We refer to this existing solver as the full collisional-radiative model (CRM) solver. The goal is to retrofit the doublets into this scheme.

To match the resolving power of the new microcalorimeter X-ray missions (the *X-ray imaging and spectroscopy mission*, XRISM, and the *Advanced telescope for high-energy astrophysics*, Athena), we need to self-consistently resolve the single $np \rightarrow 1s$ lines in CLOUDY into the fine-structure j -resolved doublets within CLOUDY’s existing framework. Below we will use the following notation for the Lyman doublets. The $2p_{1/2} \rightarrow 1s_{1/2}$ line will be written as $\text{Ly}\alpha_2$ and the $2p_{3/2} \rightarrow 1s_{1/2}$ transitions as $\text{Ly}\alpha_1$. Similar notations will be used for the higher Lyman lines.

We begin with the well-known theory of radiative transfer. A beam of radiation with energy $h\nu$ propagating through a medium has an intensity I_ν that evolves according to the well-known equation of radiative transfer:

$$dI_\nu = -I_\nu \kappa_\nu ds + j_\nu ds, \quad (1)$$

where the beam has traversed a path $s \rightarrow s + ds$, j_ν and κ_ν are the emission and absorption coefficients at frequency ν respectively. Atoms, ions, and molecules can absorb and emit radiation of frequency ν , contributing to the emission and absorption coefficients as follows:

$$j_\nu = (1/4\pi)n_u A_{ul} h\nu \phi_\nu, \quad (2)$$

$$\kappa_\nu = n_l \sigma_{lu}(\nu) - n_u \sigma_{ul}(\nu), \sigma_{lu} \propto \frac{g_u}{g_l} \frac{1}{\nu_{lu}^2} A_{ul} \phi_\nu \quad (3)$$

where n_u is the population density of the level u , A_{ul} is the transition probability, u and l are the upper and lower energy levels of the transition, σ_{lu} is the absorption cross-section, and ϕ_ν is the normalized line profile.

Figure 1 shows an energy level diagram of a one-electron atom, with the key electron transitions that need to be considered. In concurrence with this figure, for the remainder of this manuscript, we will denote energy levels $1s$, $2p$ (${}^2P_{1/2}$), $2s$, and $2p$ (${}^2P_{3/2}$) simply as levels 1,2,3 and 4 respectively. The above theory reveals that first, we need only to calculate the population densities n_2, n_4 and the frequencies ν_{12}, ν_{14} of the j -resolved levels/transitions. Then CLOUDY’s existing solvers, which compute the total $1s$, $2p$, and $2s$ populations, would self-consistently produce the correct line intensities. The equation of detailed balance in steady state shows us how n_2, n_4 relates to the population density n_{2p} already in

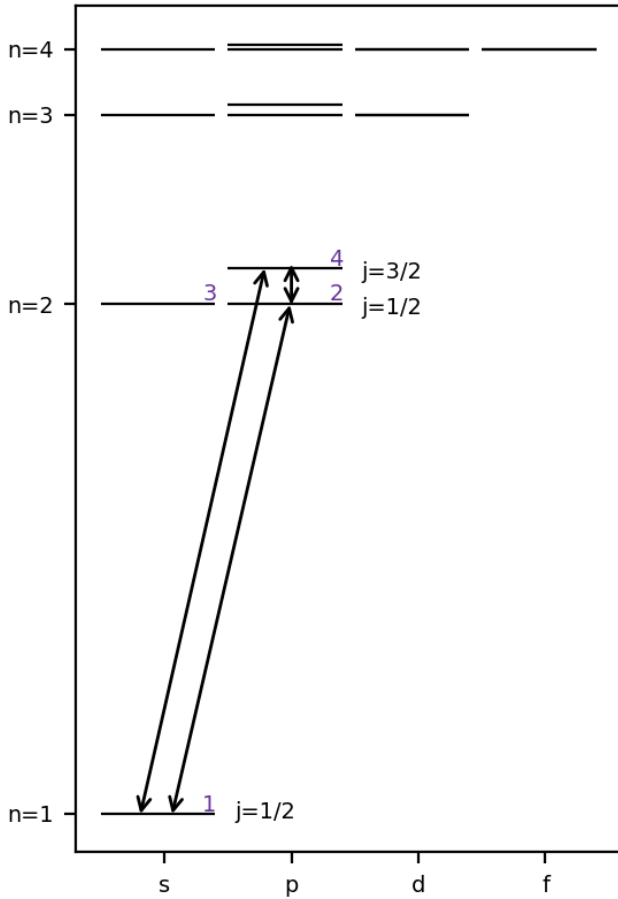


Figure 1. Energy-level diagram showing the fine-structure levels of angular momentum quantum number $l = 1$. The level ordering is consistent with energy levels of lighter H-like species. For higher- Z one-electron atomic species, the energy of the level $2s$ (${}^2S_{1/2}$) is higher than that of $2p$ (${}^2P_{3/2}$). This energy swap is not predicted in Yerokhin & Shabaev (2015), which is the paper NIST uses for the $2s$ and $2p$ (${}^2P_{3/2}$) states for high Z .

CLOUDY,

$$n_{2p}A_{2p,1}\beta_{net} = n_4A_{4,1}\beta_4 + n_2A_{2,1}\beta_2, \quad (4)$$

where β is the escape probability accounting for radiative trapping effects. In Section 3.4, we detail our population density determinations for the j -resolved states.

The line frequencies ν_{12}, ν_{14} are set by the fine-structure resolved level energies. Spin-orbit coupling combined with relativistic and quantum electro-dynamic effects lift the degeneracy in the nl energy levels, splitting 2P levels into two (Bethe & Salpeter 1957). Section 3.1 discusses the complete energy calculations and the physics behind fine-structure levels.

Next, we need to account for line overlap in our line profile function. Equations 2, 3 and the escape probability β make use of a single line profile for the $2p \rightarrow 1s$ transitions. Shaw et al. (2005) developed a multi-grid approach where the

gas opacity is treated with two energy meshes. Much of the continuum radiative transfer is done with our “coarse continuum”, which has a resolving power of order 10^3 . The fine opacity mesh has far higher resolution and resolves the line profiles, allowing for an automatic treatment of line overlap. This was necessary due to the density of electronic H_2 lines at photodissociation energies.

Section 3.5 discusses overlapping lines in greater detail for the H Ly α line and using the sum of the optical depths of the j -resolved lines for Ly β and higher lines. The calculation of the j -resolved escape and destruction probabilities and their relation to the non- j resolved lines, is also presented here.

Since resolving $np \rightarrow 1s$ for all Z and n is not needed in every case, we use the astrophysical context and the energy spectral resolution of XRISM and Athena to select the reported Z, n . We use a default spectral resolution to resolve the fine-structure doublets and introduce a new user command to change it. This is discussed in Section 3.2.

We now know the individual opacities for the j -resolved lines and need to get this information into CLOUDY’s main nl solver self-consistently. For each microphysical process that CLOUDY simulates (such as line trapping, continuum fluorescence, destruction by background opacities), we redirect the main solver to use the j -resolved physical quantities (populations, energies, opacities) for each Z and n .

The energy of the $2s$ (${}^2S_{1/2}$) level is very close to the $2p$ (${}^2P_{1/2}$) level. Most $2s$ decays produce two-photon emission but a magnetic dipole single photon transition $2s_{1/2} \rightarrow 1s_{1/2}$ (hereafter the M1 line) is possible. Appendix 3.7 compares the two- and one-photon rates. The M1 line has an energy that is close to the j -resolved transition $2p_{1/2} \rightarrow 1s_{1/2}$. Thus, when resolving the fine-structure doublets as discussed above, there is some ambiguity with the M1 line resulting in M1 line contributions to the intensity of the j -resolved doublet, the classical Ly α transition. We disambiguate these lines by giving the M1 lines in CLOUDY a new line label. This is further discussed in Section 3.7.

The $2p$ fine-structure levels of two-electron systems are singlets and triplets. Our model two-electron atom resolves these into nl -resolved states for all levels. The 2^3P level is split into its three j levels since these are important X-ray diagnostics for higher- Z elements (Porter & Ferland 2007). As such, the treatment of the He-like “extra” Lyman lines remains unchanged from the previous versions of the code. The fine-structure splitting of subordinate lines is far smaller than for the resonance lines so they will either be in the unobservable XUV or unresolvable in astrophysical applications.

3. ATOMIC STRUCTURE AND RATES

The CRM solver adopts nl -resolved energy levels. To fit the nlj -resolved fine structure calculations into the existing nl -resolved infrastructure, we take the following steps. First,

we will duplicate the pre-existing one-electron ‘‘extra’’ Lyman line structure to be used for the two j -resolved arrays np_j , for $j = 1/2$ and $j = 3/2$. Using the CRM nl level populations, we populate the upper levels of the nlj array, with the appropriate population densities (further discussed in Section 3.4). The CRM solver evaluates the total doublet emission lines from np to $1s$. We recover the nlj -resolved line optical depths from the known relationships among the Einstein rate coefficients.

The astrophysical context and instrumental limits determines which H-like ions and levels should be fine-structure resolved. It is also necessary to determine whether j -changing collisions are important in the density domain utilized by CLOUDY. The following subsections discuss our analysis, and determinations of each of these values.

3.1. Energy Calculations

3.1.1. Fine-Structure Splitting

Consider a single electron orbiting an atomic nucleus of charge Z . An accelerating charge sets up a magnetic field. This field exerts a torque on the magnetic moment of the nucleus, causing it to align with the field. Hence the general Hamiltonian of the electron in the magnetic field of the nucleus is,

$$H = \mu_e \cdot \mathbf{B}_N. \quad (5)$$

The magnetic field of the nucleus can be written in relation to the orbital angular momentum of the electron. In the rest frame of the electron, the magnetic field can be approximated by a current loop. The current is given by $I = Ze/T$, where T is the orbit period. Since this is the same orbital period of the electron which relates to its orbital angular momentum, $\mathbf{B}_N \propto \mathbf{L}_e$.

The magnetic dipole moment of a spinning charge is related to its spin angular momentum. So, we have $\mu_e = -\frac{e}{m} \mathbf{S}_e$. Hence $H \propto \mathbf{S} \cdot \mathbf{L}$, which is the spin-orbit interaction. The eigenvalues of this term are given by $j(j+1) - l(l+1) + s(s+1)$. For an electron, we have $s = 1/2$, so there is no dependence on s . Additionally, the relativistic correction cancels out the orbital angular momentum quantum numbers, leaving only a dependence on the quantum number j . The level energy including all these corrections with the fine structure included are,

$$E_n^0 + E_{nj}^{FS} = m_e c^2 \left[1 + \left(\frac{\alpha Z}{n - k + \sqrt{k^2 - \alpha^2 Z^2}} \right)^2 \right]^{-\frac{1}{2}} - m_e c^2 \quad (6)$$

where, $j \in \{|1/2 - l|, \dots, (1/2 + l)\}$, $k = j + 1/2$, n is the principal quantum number, α is the fine structure constant and m_e is the mass of the electron. E_n^0 is the unperturbed energy:

$$E_n^0 = -\frac{\mu}{m_e} \frac{Z^2 Ry}{n^2}. \quad (7)$$

Here $Ry = hcR_\infty$ is the infinite-mass Rydberg unit of energy (Bethe & Salpeter 1957), and $\mu = m_e m_N / (m_e + m_N)$ is the reduced mass of the electron, where m_N is the nuclear mass. This interaction can be thought of as a perturbation that partially lifts the degeneracy of the energy states by splitting the levels with different orbital quantum number l . For all one-electron systems, the 2P state ($l = 1$) is resolved into a doublet with $j = 1/2, 3/2$.

3.1.2. np Level Energy Corrections

We use the following approximation for the binding energy E_{np} of an np electron in a hydrogen-like atom. Here we retain the lowest-order correction terms, which will give sufficient accuracy for our needs.

$$E_{np} = E_n^0 + E_{nj}^{FS} + E_{n,l=1,j}^{LS} + E_{nj}^M, \quad (8)$$

For our calculations, we use the ionizing potentials of the one-electron ion already given within CLOUDY (as taken from NIST) to determine E_n^0 . The NIST ionization potentials adopted by CLOUDY are only n -resolved, and does not include Lamb shift and other corrections. E_{nj}^{FS} is the fine-structure correction that resolves the levels with different j given in Eq. 6.

NIST ionization potentials are accurate and include corrections such as the Lamb shift. Equation ?? double counts the Lamb shift. This introduces negligible error since the shift is so much smaller than the ionization potentials (Z^2 Ryd). The correction is more important for line energies, which are the difference in energy between two levels.

$E_{n,l>0,j}^{LS}$ is the Lamb Shift correction which resolves the levels with different l ,

$$E_{n,l>0,j}^{LS} = \frac{8Z^4 \alpha^3}{3\pi n^3} Ry \left[\log \frac{Z^2 Ry}{K_0(n, l)} + \frac{3}{8} \frac{c_{lj}}{2l + 1} \right], \quad (9)$$

$$c_{lj} = \begin{cases} (l+1)^{-1}, & j=1+1/2, \\ -l^{-1}, & j=1-1/2. \end{cases} \quad (10)$$

where $\log K_0(n, l = 1)/Z^2 Ry$ is the Bethe logarithm. The numerical value of $K_0(n, l = 1)$ is difficult to evaluate for a large number of n , so we developed an approximation of the Bethe logarithm as discussed in Appendix A. For the present purpose, this sufficiently satisfies the present and future instrumental needs as discussed in the following section.

Lastly, E_{nj}^M is the nuclear mass recoil correction

$$E_{nj}^M = m_e c^2 \frac{m_e}{m_N} \frac{(\alpha Z)^2}{2N^2} - \mu c^2 \left(\frac{m_e}{m_N} \right) \frac{(\alpha Z)^2}{2n^2} \quad (11)$$

$$N = \left(\left(n - k + \sqrt{k^2 - \alpha^2 Z^2} \right)^2 + \alpha^2 Z^2 \right)^{1/2} \quad (12)$$

where $k = j + 1/2$ as before (Yerokhin & Shabaev 2015).

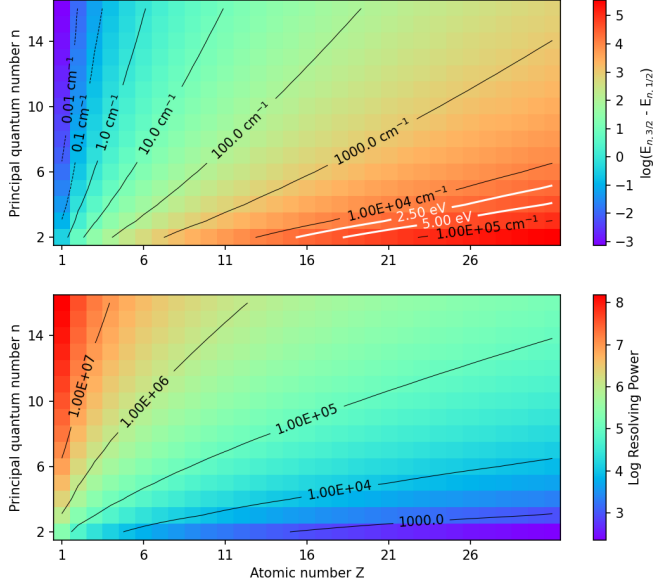


Figure 2. *Top:* Contour plot of energy separation between the np ($^2P_{1/2}$) and np ($^2P_{3/2}$) levels. The white plot lines indicate the spectral resolution of the current microcalorimeter mission *XRISM* ($R \sim 5$ eV) and future mission *Athena* ($R \sim 2.5$ eV). *Bottom:* Contour plot showing the resolving power required to distinguish between the $np_{1/2} - 1s_{1/2}$ and $np_{3/2} - 1s_{1/2}$ transition energies, where $E_{1s_{1/2}} = 0$. For both plots the y-axis is the range of principle quantum numbers used in *CLOUDY* calculations, and the x-axis is the range of elements with atomic number Z used.

3.2. Energy Resolution & Accuracy

Figure 2 shows a contour map of the spectral energy resolution (top panel), and the required resolving power (R) (bottom panel) for fine-structure splitting in the 2P shell of nuclear charge ranging from H to Zn ($Z=30$) and n ranging from 1 to 16. The energy difference in the split fine-structure levels become rapidly smaller at higher n levels, but rapidly larger with heavier atomic nuclei.

XRISM has an energy resolution of 5 eV for the energy range 0.3-12 keV, while *Athena* is expected to have a resolution of 2.5eV (*XRISM Science Team 2020*). So to meet the upcoming instrumental requirements, according to figure 2, we need to resolve the 2P shells into doublets for atoms heavier than phosphorus ($Z=15$) and for $n < 5$. However, we use Equations 6-12 to calculate the energies for all Z and n , and report only those lines resolvable by a given spectral resolution. The reported j -resolved lines are determined within the code, using a test comparing the energy difference between the two fine-structure levels to the desired spectral resolution. By default we implement a spectral resolution that is a factor of 10 better than *Athena*'s predicted resolution (i.e., we use a resolution of $2.5 \text{ eV}/10 = 0.25 \text{ eV}$), for the Lyman lines. We also introduce a new command allowing users to alter

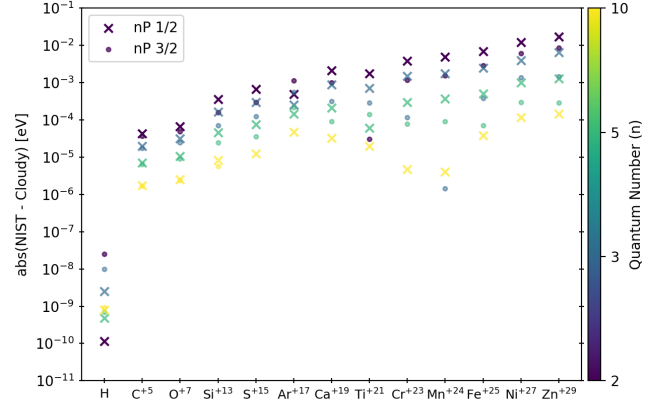


Figure 3. Energy scale accuracy of the updated np ($^2P_{1/2}$) and np ($^2P_{3/2}$) levels for H-like species in *CLOUDY*, using NIST as the authority. The expected accuracy for *XRISM* is 0.5 eV, which is well above those for any of our new H-like np_j energy calculations. The dots indicate the accuracy for $j = 1/2$, and crosses indicate those for $j = 3/2$. The colors going from purple to green indicate increasing principle quantum number n .

this default resolution (See Hazy 1, Section 12.4.12 Database H-like Lyman extra resolution, of the C25 release).

Additionally, *XRISM* has an energy scale accuracy of 0.5 eV (*XRISM Science Team 2020*). The spectral energy resolution reflects the instrument's ability to differentiate between two closely spaced energies, while the accuracy resembles the instrument's ability to detect the energy of a photon as close to its true value as possible. Figure 3 provides the difference between our total level energies and those in NIST, in units of eV for various one-electron atoms. We find that our largest energy error is approximately 0.01 eV, which is more than a factor of 10 better than *XRISM*'s energy accuracy.

This treatment fulfills the energy accuracy and resolution requirements for the up-coming X-ray missions and beyond. We also, prevent fine-structure splitting of the 2P level in hydrogen and helium, due to the instrumental limitations as seen from Figure 2.

3.3. Transition Rate Coefficients

CLOUDY uses non-relativistic calculations to determine radiative transition rate coefficients (a.k.a Einstein A values)(*Drake 2006*). These computations are not j -resolved, since the correction factors evaluate to unity in our simple case. We leave them as they are for now. Future work will involve including relativistic corrections to the *CLOUDY* computed transition probabilities. The current Einstein A's in *CLOUDY* differ from the NIST values which include relativistic corrections, by at most ~ 2 per cent (*Jitrik & Bunge 2004*), this accuracy is sufficient for our current instrumental needs.

3.4. Populations and Intensity Ratios

The intensities of the emission line are determined by the population density of the corresponding upper level u of the transition (n_u) and the rate of spontaneous emission (A_{ul}) of the transition $u \rightarrow l$. So, to determine the np fine-structure line intensities, we need to first determine the population densities of the $np_{j=1/2}$ and $np_{j=3/2}$ levels. Here we discuss the prescriptions for $n = 2$ levels for simplicity, however, the same framework is extended for levels $n > 2$.

The presence of fine-structure transitions is determined by the density of the ionized gas (n_{gas}). In steady state, $\frac{dn_u}{dt} = 0$ results in two possible limits based on how the ionized gas density compares with the critical density (n_{crit}),

$$n_{\text{crit}} = A_{ul} / q_{lu}. \quad (13)$$

In the low-density limit ($n_{\text{gas}} < n_{\text{crit}}$), radiative emission is faster than the rate of collisions. Hereby, we will call this the radiative limit. Here, the density of our gas is sufficiently low enough to ignore collisional j -changing transitions, so the j -changing transitions can be neglected. Here the population ratio is related to the rates at which the nlj levels are populated.

In the high-density limit collisions are much faster than spontaneous emissions ($n_{\text{gas}} > n_{\text{crit}}$). We will refer to this limit as the collisional limit. Here, n_2/n_4 becomes equal to the ratio of the statistical weights of the corresponding levels. Figure ?? shows n_{crit} for proton- and electron-impact collisions for four one-electron ions (C VI, Mg XII, S XVI, Ar XVIII), and Figure ?? shows the rate coefficients used to compute n_{crit} . We provide electron rates for the $2 \rightarrow 1$ transition (q_{12}) for a more complete comparison. The lack of proton collision rate coefficients is a pressing atomic data need for the next generation of X-ray observatories. For nearly degenerate energy levels, slow collisions are more effective than fast ones (Jackson 1998, Section 13.1). So, electron collisions are less important because of their greater speed in a thermal gas. Extensive electron fine structure collision data are given in Mao et al. (2022). These were used to calculate the electron rates q_{ul} with the following (Osterbrock & Ferland 2006)

$$q_{lu} = \frac{8.63 \times 10^{-6} \Omega(l, u)}{g_u T^{1/2}} \text{cm}^3 \text{s}^{-1}, \quad (14)$$

where g_u is the statistical weight of the upper level, and T is the temperature of the ionized gas. However, we expect proton rates to be more important at lower temperatures (Bahcall & Wolf 1968; Zygelman & Dalgarno 1987). We can see this by extrapolating the plot-lines in Figure ??, where for most one-electron species $q_{24} < q_{24}^p$ at lower T . A general theory for ion-ion collisions is given by Pengelly & Seaton (1964); Walling & Weisheit (1988), while Igarashi et al. (2003) give cross sections of proton-impact excitation between the $n = 2$ fine-structure levels of hydrogenic ions.

CLOUDY is designed to operate over a very broad range of densities, going from the low-density limit up to LTE, $n \geq 10^{20} \text{cm}^{-3}$ depending on the ion, Figure ?? confirms we may reasonably assume the radiative limit and that j -changing collisions can be ignored for densities below 10^{20}cm^{-3} . The critical densities for all hydrogenic species heavier than C VI shown in Figure ?? is above 10^{20}cm^{-3} . The gas densities of typical H II regions are $\sim 10^4 \text{cm}^{-3}$ which is well below the above-mentioned values of n_{crit} . This introduces a new uncertainty. In this low-density limit, the j -resolved $2P$ level populations are determined by the rates that the various j -resolved levels are populated by. That, in turn, would require fine-structure resolved rate coefficients for recombination, collision, and radiative transitions that populate the j levels. Those data are yet to be implemented into CLOUDY.

We assume that the j -resolved population densities to scale according to the ratio of statistical weights, compared to the population density calculated for the unresolved lines,

$$n_{npj} = \begin{cases} n_n \left(\frac{g_{np}}{2n^2} \frac{g_{npj}}{g_{np1/2} + g_{np3/2}} \right), & \text{collapsed states} \\ n_{np} \left(\frac{g_{npj}}{g_{np1/2} + g_{np3/2}} \right), & \text{resolved states} \end{cases} \quad (15)$$

where $g_{np} = 2(2l + 1) = 6$ is the statistical weight for the l -resolved levels with $l = 1$, $g_{npj} = 2j + 1$ are the statistical weights of the j -resolved levels and $j = \frac{1}{2}, \frac{3}{2}$.

3.5. Radiative Trapping and Line Overlapping

Nearly all lines in CLOUDY are instances of a C++ object, allowing these lines to be treated with a common code base. Line transfer is done using the escape probability formalism (Kalkofen 1984; Elitzur 1992). This unified code base allows most lines to include radiative trapping and fluorescence, and line thermalization. The code uses various theories to calculate the escape probability, depending on the classification of the line (see, e.g., Section 3.4 in Rutten 2003). For hydrogen Ly α , the code uses fits to the results presented in Hummer & Kunasz (1980, hereafter HK80), which takes line destruction by background opacities into account.

In general, radiative damping can be important for permitted lines in high- Z elements. The Voigt profile function accounts for this broadening, in addition to broadening of the upper and lower levels of the transition and thermal broadening. CLOUDY calculates the Voigt profile using the theory described in Wells (1999) and Hjerting (1938). This routine is very accurate.

The HK80 theory implicitly assumes the line to be single, i.e., it does not consider the case where lines overlap, as occurs for the two fine-structure components of the Ly α line. In the following, we will show how we modified the theory to deal with this problem.

The starting point of the theory presented in HK80 is the b_{HK} parameter, the ratio of background continuum (k_c) to

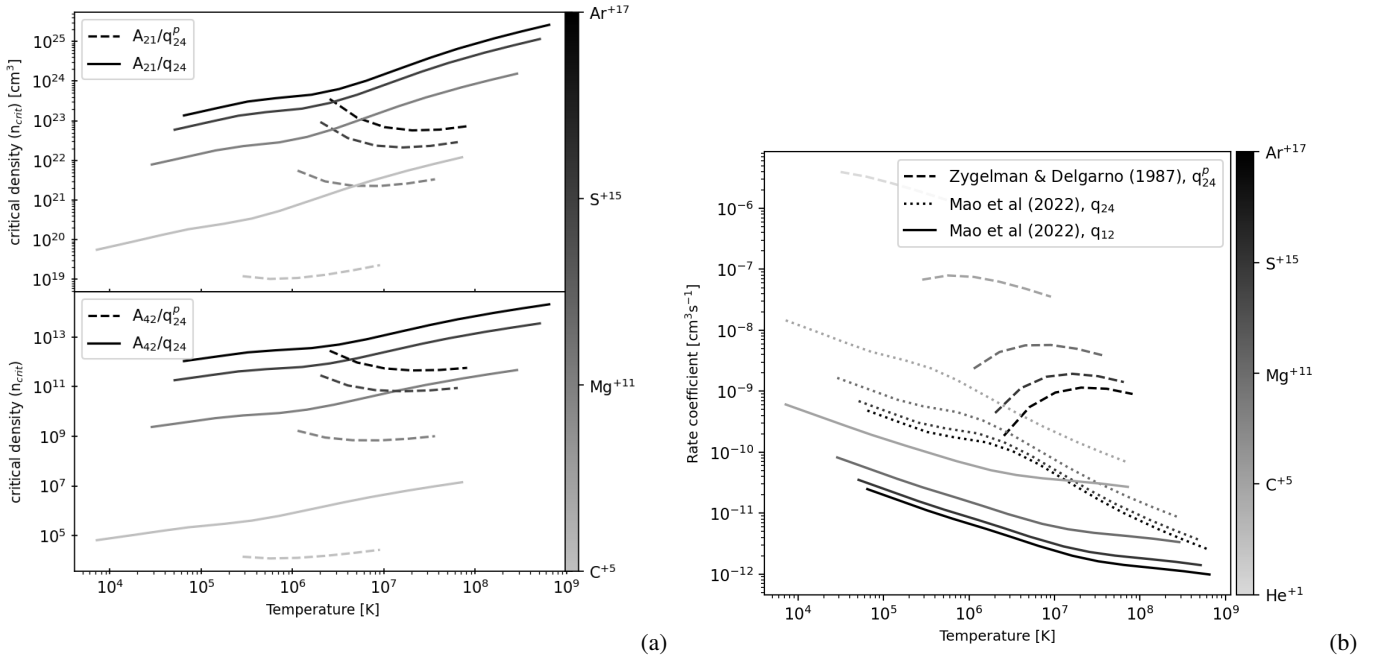


Figure 4. (a) n_{crit} for proton- and electron-impact collisions for four one-electron ions. (b) rate coefficients used to compute n_{crit} as a function of temperature for the one-electron ions with proton-impact collisional data.

line opacities, which is defined as (Eq. 2.7 of HK80):

$$\beta_{HK} \equiv k_c/k_L, \quad (16)$$

CLOUDY is designed to work over a very broad range of physical conditions, including cases where the continuous opacity is large. We work with a modified version, the ratio to total opacity,

$$\beta'_{HK} = k_c/(k_c + k_L). \quad (17)$$

For most clouds, the two versions of β_{HK} are nearly equal. β'_{HK} is the probability that a photon will be absorbed and destroyed by background opacity rather than by line scattering.

The frequency-dependent line opacity k_L is defined as (Eq. 2.3 of HK80):

$$k_L = \frac{N_l B_{lu} h \nu_0}{4\pi \Delta}, \quad (18)$$

where N_l is the population of the lower-level, B_{lu} is the einstein B coefficient of the transition $u \rightarrow l$, h is the Planck constant, ν_0 is the central frequency of the line, and Δ is the Doppler width of the line. This can be simplified to Eq. 8 of Gunasekera et al. (2023):

$$k_L = N_l \kappa_L \sqrt{\pi} / \Delta_\nu, \text{ where } \Delta = \frac{\nu_0}{c} \Delta_\nu. \quad (19)$$

CLOUDY uses a multi-grid approach to fully resolve overlapping lines on a “fine continuum” while doing much of the physics on a “coarse continuum” (Shaw et al. 2005). The

fine continuum attempts to resolve most line profiles while the coarse continuum has a lower resolution. The frequency-dependent line profile $k(x)$ that needs to be entered into the fine-opacity array is given by:

$$k(x) = k_L \frac{1}{\sqrt{\pi}} H(a, x) = \frac{N_l \kappa_L}{\Delta_\nu} H(a, x), \quad (20)$$

where a and x are defined in HK80, and $H(a, x)$ is the Voigt function defined by Eq. 2.4 of the same paper. Since $H(a, 0) = \exp(a^2) \text{erfc}(a) \approx 1$ for $a \ll 1$, we get:

$$k_L \approx k(0) \sqrt{\pi}. \quad (21)$$

This latter equation can be used to generalise the treatment for overlapping lines. Instead of using Eq. 19 to calculate β_{HK} , as was done in previous versions of the code², we will now use Eq. 21. This version will automatically treat line overlap when $k(0)$ is taken from the fine opacity array after all lines have been entered. One drawback of this approach is that, in general, the overlapping lines will no longer have the shape of a Voigt profile, which is implicitly assumed by HK80. However, since the fine-structure components are very

² In the process of implementing this, we discovered a bug in CLOUDY versions C23.00 and before where the factor $\sqrt{\pi}$ was placed in the denominator rather than the numerator. This bug only affected the calculation of β_{HK} (and hence the destruction probability), not the line profile given in Eq. 20. This was fixed in version C23.01 (Gunasekera et al. 2023).

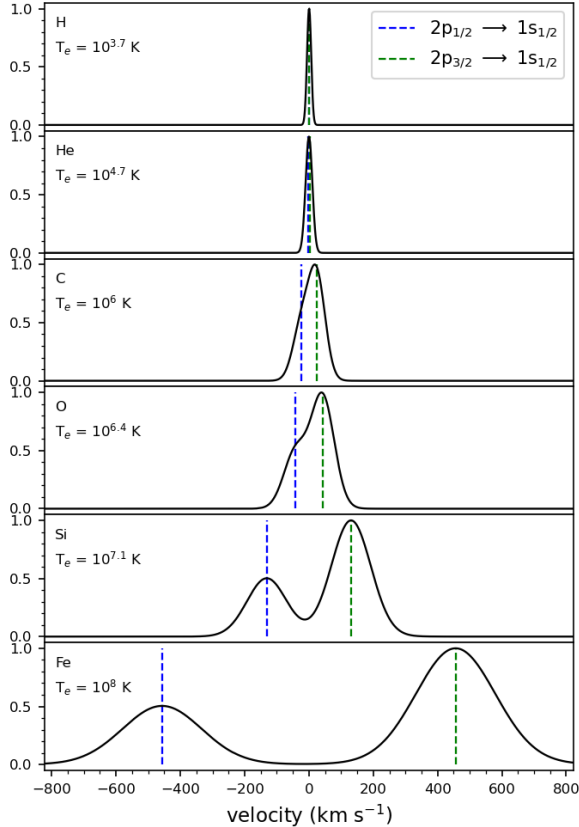


Figure 5. Normalized line opacities as a function of line-of-sight velocity for several one-electron $2p$ fine-structure doublets, at a spectral resolution of 0.25 eV, showing the doublet splitting increasing with increasing Z . The blue and green dashed lines indicate the position of the $j = 1/2$ and $j = 3/2$ lines, respectively. The temperature of the gas is indicated in the top left corner of each panel and corresponds to the temperature where the ion’s abundance peaks in collisional equilibrium. Line profiles tend to become sharper as the nuclear mass increases but broader as the temperature increases.

closely spaced in H I Ly α , in most environments the H Ly α lines will strongly dominate over other blended lines.

Figure 5 shows the increasing separation between the fine-structure doublets of one-electron species. The doublet separation is smaller than the thermal width for small Z but the lines are quite distinct at large Z . The low- Z elements can be treated as single lines, while the high- Z and low- n lines are treated as two separate lines.

The calculations of the destruction probabilities due to the continuum opacity suffer the same problem of not allowing for overlapping lines. It is the lines from low- Z ions that exhibit line overlapping. For these lines, we simply treat the doublets as two separate lines by summing the opacity of the two j -components to calculate both the escape and destruction probabilities. An overlapping line is considered to be one where the difference between the Doppler velocities of the two j -resolved lines is less than the Doppler width of

the single line ($\Delta_v < \Delta$). Additional tests on the damping constant for the one-electron doublets yield that much of the line broadening that increases with Z is a result of radiative damping.

Then using Equation 4 and the fact that $A_{4,1}$ and $A_{2,1}$ are identical to $A_{2p,1}$ (see Section 3.3), we calculate the unresolved escape and destruction probabilities using those for the j -resolved lines,

$$\beta_{2p,1} = \frac{1}{3}\beta_{4,1} + \frac{2}{3}\beta_{2,1}. \quad (22)$$

3.6. Atomic Energy Levels

Due to the high resolution of spectra that will be observed with microcalorimeter missions such as XRISM and Athena, a larger number of atomic high-energy levels ($n > 100$) become relevant in the CLOUDY calculations. As such, we increase the number of levels included in the H-like Fe atom by default to 55.

Additionally, CLOUDY by default includes only the energy levels from the Chianti v10.0.1 atomic database which have energies below the ionization potential of the corresponding ion (we refer to these as auto-ionizing levels) (Gunasekera et al. 2022). However, with spectral resolutions $R > 1000$ even lines produced by transitions involving autoionizing levels will be observed. The work in Gunasekera et al. (2022) provides a CLOUDY-compatible version of the Chianti 10.0.1 database that includes all levels in the original Chianti database, available to be downloaded from <http://data.nublado.org/chianti/>, with filename “chianti_v10.0_full”. Note, that CLOUDY users should use the set `UTA off` command to ensure that the auto-ionizing lines are not double counted.

3.7. The magnetic dipole line

CLOUDY has long predicted the M1 line (the magnetic dipole $2s_{1/2} \rightarrow 1s_{1/2}$ transition), which has a transition energy and frequency very close to that of the $2p_{1/2} \rightarrow 1s_{1/2}$ transition. We update the transition energies of the M1 lines to those published in Yerokhin & Shabaev (2015). This accounts for the appropriate Lamb shift energy corrections the level and disambiguates the $2s_{1/2}$ and $2p_{1/2}$ level energies. Furthermore, CLOUDY identifies specific line transitions by matching the line label and the line wavelength. The label has the typical four-character form “LLXX”, where “LL” is the usual one- or two-letter element symbol, and “XX” is the ion charge, while the line wavelength has up to 6 significant figures. Thus, for transitions involving the same atom/ion with sufficiently close wavelengths, CLOUDY cannot disambiguate between the two lines. This was the case for the M1 line and the $2p_{1/2} \rightarrow 1s_{1/2}$ transition for low Z . We now disambiguate the M1 line from the fine-structure Ly α line within CLOUDY, by extending the line label of the former to “LLXX M1”.

The relative contributions of two-photon E1 and single-photon M1 transitions also depend strongly on the nuclear charge, as discussed in Appendix B. The M1 transition is predicted to dominate for heavy elements ($Z > 40$, Sobelman 1979) such as those produced in neutron star mergers.

4. X-RAY SPECTRAL DIAGNOSTICS

We present CLOUDY calculated results, for a model of the Perseus Cluster obtained from Chakraborty et al. (2020b). Perseus being the prototypical cool-core cluster, and one of the brightest ones observed, provides an excellent model for study. Figure 6 shows total emission spectra, from both before and after resolving the Lyman lines. The model is a collisionally-ionized plasma with a constant temperature of 4.7×10^7 K, hydrogen density of $10^{-1.5} \text{ cm}^{-3}$, and 0.65 dex solar metallicity. A microturbulent velocity of 150 km s^{-1} is included to account for line shielding and pumping. The energy range, 0.4 - 10 keV, is covered by the XRISM mission, and includes the important Fe Ly α doublet. The y-axis has been scaled by the thickness of the cloud Δr , since the line intensities will depend linearly on the Δr for optically thin transitions with no external radiation field.

With the default spectral resolution implemented (1/10 of Athena's resolution, 0.25 eV) we see that CLOUDY now predicts Ly α doublets for all H-like species heavier than nitrogen. Since this update provides an energy accuracy beyond the current and future X-ray microcalorimeter spectral resolution (as shown by Figure 3), the improved CLOUDY spectra will be in excellent agreement with microcalorimeter observations.

The following subsections use the Perseus cluster core model presented above. We expand the model for the range of hydrogen column densities that occur in X-ray emitting clouds, $18 < \log N(\text{H}) < 25$. The input scripts and the ensuing figures are available in gitlab.nublado.org/cloudy/papers. The choice of including Ca XX in the following subsections is justified by the fact that XRISM/Resolve will resolve Ly α doublets only for elements at least as heavy as calcium (Gunasekera et al., A&A, submitted).

4.1. A Column Density Indicator

We present the classical Baker & Menzel (1938) Case A (small N) to Case B (large N) limits (Osterbrock & Ferland 2006; Chakraborty et al. 2021), for the Perseus cluster core model. Figure 7 shows the unresolved Fe Ly α , the j-resolved Ly $\alpha_{1,2}$ doublet, along with their counterpart that is predicted by the previous version of CLOUDY, C23.01. The figure shows sensitivity of the Fe Ly α I to H column densities $> 10^{22} \text{ cm}^{-3}$. The j-resolved doublet splitting calculations reveal that Ly α is much stronger here compared to the C23.01 model. There was a clear underestimation of the intensity of the Fe xxvi Ly α line predicted in C23.01. This arises from an underestimation of the continuum pumping for the single line compared to the

sum of the two j-resolved lines, with smaller optical depth and opacity. As we will show in Section 4.2, the Case A to B transition enhances the Ly α line much more rapidly than Ly β . This behavior results from two competing processes. As $N(\text{H})$ increases, so does the line optical depths. Scattering Ly β photons have a finite probability of being absorbed and re-emitted as Ba α followed by Ly α , intensifying the Ly α line. Conversely, the destruction of higher Ly α lines results in Ly β and other lower series photons (Netzer et al. 1985; Hubeny & Mihalas 2015). The stronger Ly α line than predicted in C23.0, implies that Ly β destruction dominates over Ly α destruction much more than previously calculated.

4.2. Transitions from Case A to Case B

The higher- n Lyman lines also provide a column density indicator. Fig 8 shows the predicted Ly β /Ly α intensity ratio as a function of the column density (bottom panel), along with optical depth per unit column density of each line (top panel). We report both Ly β ($n = 3 \rightarrow 1$) and Ly α ($n = 2 \rightarrow 1$) as the multiplet sum in this Figure.

The dependencies of calcium and iron ionization are complex. The $\tau/N(\text{H})$ of an emission line changes with total column density, as shown in the top panel of Figure 8. This reveals that the mean ionization changes as $N(\text{H})$ increases. Large column densities have large optical depths, resulting in trapped line radiation within the cloud. These trapped lines, scatter many times photoionizing other elements, affecting the mean ionization of the cloud. Here, the ionization of the H-like Fe increases with $N(\text{H})$, while that of H-like Ca decreases, resulting in the difference in the Ly β /Ly α trends between Fe XXVI, and Ca XX with $N(\text{H})$.

The Case A to B transition increases the optical depth in the lines. Each Fe Ly β photon scattering has a $\sim 11\%$ probability (this probability comes from the Einstein $A_{u,l}$ ratio $\frac{A_{3p,2s}}{A_{3p,1s} + A_{3p,2s}}$) of being converted into Ba α ($n = 3 \rightarrow 2$) followed by Ly α . Multiple scattering causes the Fe XXVI Ly α to grow stronger and Ly β weaker. This Fe Ly α to Fe Ly β conversion begins as Ly β weakens at $N(\text{H}) \sim 10^{21} \text{ cm}^{-3}$ and provides a column density diagnostic. However, the Ca Ly β /Ly α ratio, for this particular model, exhibiting a maximum as a function of $N(\text{H})$ is not ideal as a column density indicator.

4.3. Case C to Case B

Case C is the limit where the Ly α lines are optically thin and the incident radiation field can pump the lines (Baker et al. 1938). This fluorescent excitation makes the lines stronger (Ferland 1999b). It occurs in photoionized clouds with lower column densities. As the cloud column density increases, the Ly α line optical depth increases and the transition becomes self-shielded from the incident radiation field. The emission goes over to the Case B limit (Baker & Menzel 1938; Chakraborty et al. 2021).

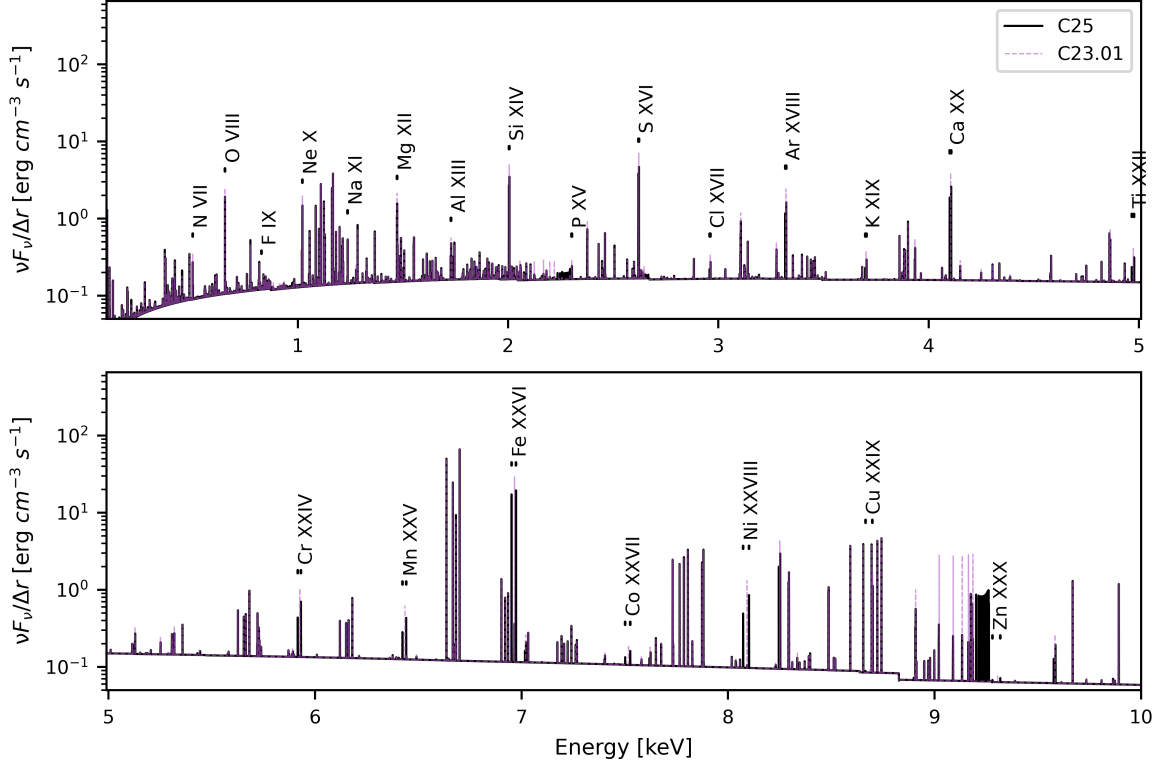


Figure 6. A CLOUDY simulation of the Perseus Cluster core with fine-structure doublets resolved for the one-electron ions. The black plot includes revisions that will appear in the C25 release, including the split fine-structure lines of one-electron species.

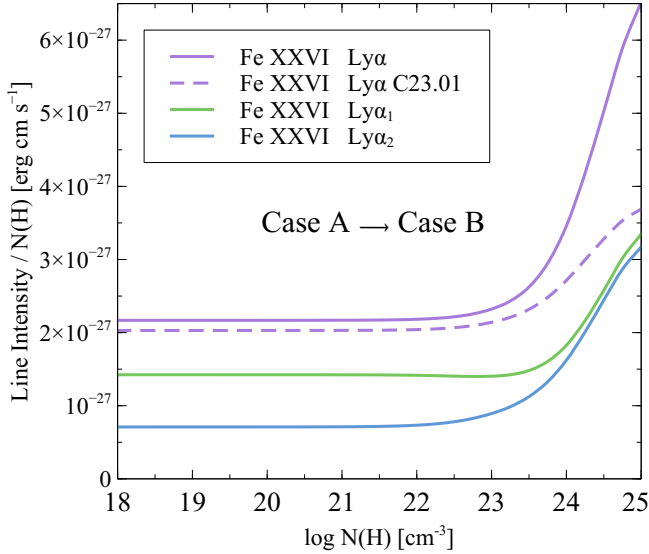


Figure 7. This shows the intensity of the Fe XXVI $\text{Ly}\alpha_1$ and $\text{Ly}\alpha_2$ lines, as well as the new unresolved $\text{Ly}\alpha$, alongside the unresolved $\text{Ly}\alpha$ as predicted using C23.01. We show the individual line intensities divided by the gas column density as a function of column density.

Figure 9 shows a series of calculations based on those shown in Figures 7 and 8. It assumes a constant gas kinetic temperature of 4.7×10^7 K for simplicity but is also

exposed to a powerlaw SED with an ionization parameter of $\log U = 3$. This radiation field is strong enough to pump the $\text{Ly}\alpha$ lines but not so strong as to change the ionization of the cloud. This is done to expose the essential physics and is not meant as a realistic model of a photoionized cloud. In a true photoionized cloud, the kinetic temperatures and ionization would change as a function of column density, obfuscating the essential physics.

5. CONCLUSIONS

With the launch of the X-ray observatory XRISM with spectral resolution $R > 1000$, the need arises for analysis tools such as CLOUDY to make full use of these new data. The series of thesis papers by Priyanka Chakraborty (Chakraborty et al. 2020a,b, 2021, 2022) expanded our treatment of two-electron spectra such as Fe XXV. This project has advanced CLOUDY's one-electron iso-sequence spectral-line predictions to match that of microcalorimeter observations, in a manner that is self-consistent with the microphysics in the cloud. This paper described how one-electron spectra are predicted in CLOUDY.

We used atomic theory rather than database lookup for the atomic framework of our model atoms. This ensures completeness and extensibility. CLOUDY treats species along one- and two-electron isoelectronic sequences with a unified model. We currently include all elements between hydrogen

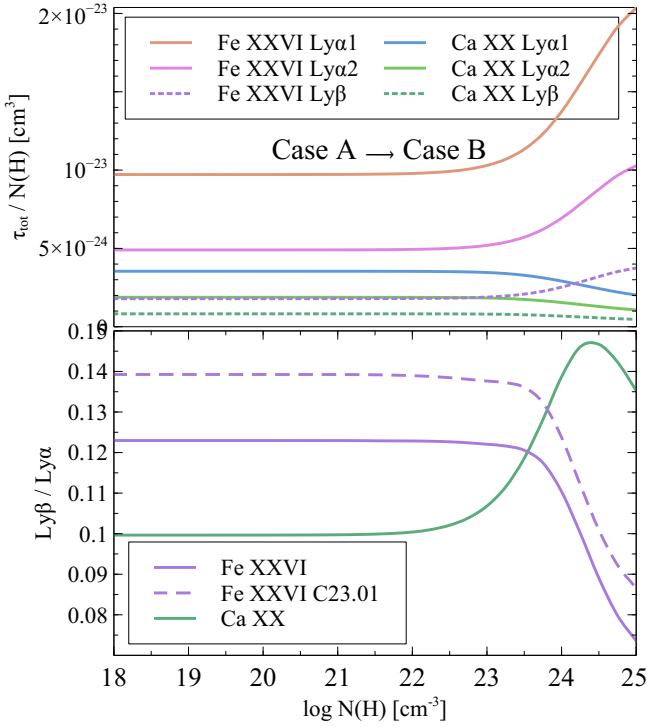


Figure 8. CLOUDY models of the Perseus Cluster core. *Top panel:* Line optical depth per unit column density, as a function of column density. *Bottom panel:* The intensity ratio of the Fe XXVI and Ca XX Ly β to Ly α lines. This is a column density diagnostic because significant line optical depths cause the Ly β to undergo multiple scattering and be transformed to the Ba α and Ly α lines. This is the classical Baker & Menzel (1938) Case A to B limit. The details of the behaviour in this figure are model dependent and are not universal.

and zinc. Our theoretical approach for the atomic data ensures that we have complete coverage of all of these elements. The treatment is general, so it will be straightforward to extend our predictions to very heavy elements such as those produced in neutron star mergers.

We extended the line redistribution theory used in CLOUDY for overlapping lines. Our framework was originally developed to treat the strongly overlapping H $_2$ electronic lines using a multi-grid approach (Shaw et al. 2005). Figure 2 shows that the degree of overlap of the one-electron doublet depends on the nuclear charge and the local velocity field. In the course of this development, we discovered a simple coding error which was described and corrected in Gunasekera et al. (2023). Our treatment remains general and can be applied to any set of overlapping lines.

We identify the lack of data for j -changing collisions within the $n = 2$ shell as the most pressing missing part of our simulations. High-quality electron collision data now exist (Mao et al. 2022). Slow-moving particles such as protons or alpha particles have the largest cross sections for j - and l -changing collisions. These exist only for a few ions. This

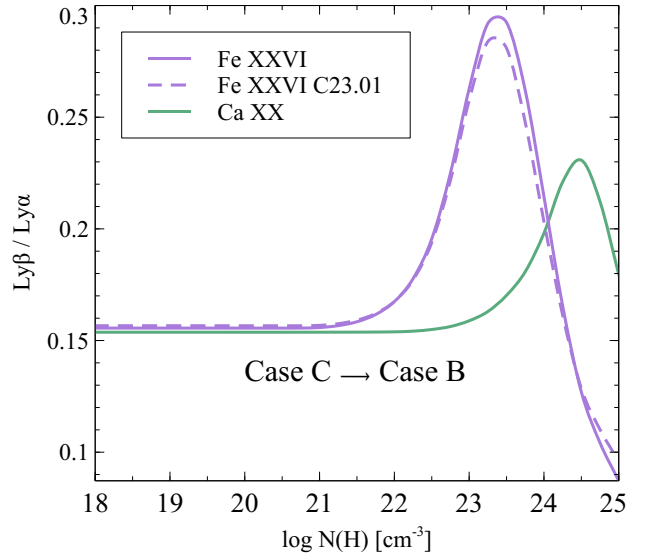


Figure 9. CLOUDY models for the Perseus Cluster core showing the intensity ratio of the Fe XXVI and Ca XX Ly β to Ly α lines. Just as Figure 8 shows the Case A to Case B transition for a collisionally ionized gas, this shows the Case C (Baker et al. 1938) to Case B transition for gas illuminated by an SED that fluoresces the one-electron Lyman series. This is also a column density diagnostic.

is discussed in Section 3.4). To include the one-electron j -resolved $2p_{1/2,3/2} \rightarrow 1s_{1/2}$ transitions in CLOUDY’s full CRM solver, and provide more accurate spectral predictions for the next generation of X-ray observations, it is essential to fill this data gap.

Lastly, Fe Ly α has long been an important measurement in X-ray observations. Fe being abundant in high-energy environments, the Ly α line can provide valuable information on the physical conditions of such regions. Using the work from this study, we show in Gunasekera et al. (A&A submitted) that the Fe Ly α_1/α_2 can be a powerful column density indicator. This work will highlight some insightful physics we can probe as a result of being able to resolve Ly α into the doublet, with XRISM observations.

The scripts for all figures presented in this paper are found in the directory named after the bibcode of the present paper, in our openly accessible repository gitlab.nublado.org/cloudy/papers. These make it easy for others to build on our modelling.

- 1 We would like to acknowledge Stefano Bianchi for his advice,
- 2 and all the participants at the CLOUDY 2024 workshop in
- 3 Tokyo, for testing this development of the code. CMG, MC
- 4 and GF acknowledges support from NASA (19-ATP19-0188,
- 5 22-ADAP22-0139) and NSF (1910687).

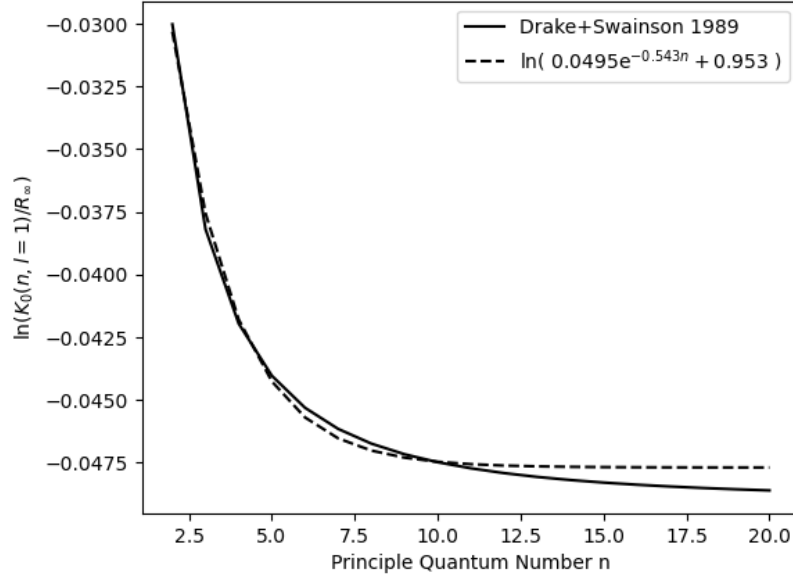


Figure 10. Derived best fit line to the $K_0(n, l)$ term of the Bethe logarithm.

APPENDIX

A. BETHE LOGARITHM

The Bethe logarithm $\ln(K_0/Z^2Ry)$ is a dimensionless quantity, where $K_0(n, l)$ represents the mean excitation energy for the Lamb Shift. It was first introduced by Hans Bethe in 1947 as part of his theory of the Lamb shift (Bethe & Salpeter 1957). For one-electron atoms with $l \neq 0$, the Bethe logarithm requires the evaluation of oscillator strengths for transitions $nl \rightarrow n', l \pm 1$. Such a calculation can become tedious when evaluating the Bethe logarithm for a large value of n . Since $K_0(n, l \neq 0)/Z^2Ry$ varies slowly with n , and does not reduce to values much smaller than unity for $n \rightarrow \infty$, we can approximate it with a negative exponential. Using an optimized curve fit to the numerical evaluations of the Bethe logarithm presented in Drake & Swainson (1990), for $l = 1$, we find the following approximation,

$$\frac{K_0(n, l = 1)}{Z^2Ry} \approx 0.0495e^{-0.543n} + 0.953. \quad (\text{A1})$$

Figure 10 shows our fit evaluated for n up to $n = 20$ and compared with the values in Drake & Swainson (1990). We find that Equation A1 provides a sufficiently good fit, especially for low $n < 10$, with a mean square error of order 10^{-7} .

B. THE ONE-ELECTRON FORBIDDEN TRANSITIONS

CLOUDY considers all elements up to $Z = 30$ (zinc). The structure of the code is designed to be readily expandable to heavier elements, so development could extend to $Z > 30$. The initial emphasis was on ultraviolet and optical spectroscopy, as driven by the instrumentation available at the time. The new generation of X-ray microcalorimeters has motivated our recent development of the one and two-electron systems at high Z . Previous papers focused on two-electron systems, with an emphasis on iron (Chakraborty et al. 2020a,b, 2021, 2022).

Here we point out an interesting aspect of the $2s_{1/2} \rightarrow 1s_{1/2}$ transition. There are no allowed (E1) single-photon transitions between these two states, but so-called “forbidden” transitions are possible. For galactic nebulae, this produces the strong HI two-photon continuum (Osterbrock & Ferland 2006). Various moments of the radiative transition rates have different dependencies on charge (Chakraborty et al. 2020b). Here, we show how the types of emission produced by the $2s_{1/2} \rightarrow 1s_{1/2}$ M1 transition change with Z . At low Z the two-photon (2E1) continuum is dominant (Osterbrock & Ferland 2006), while at very high Z the single magnetic dipole (M1) line dominates.

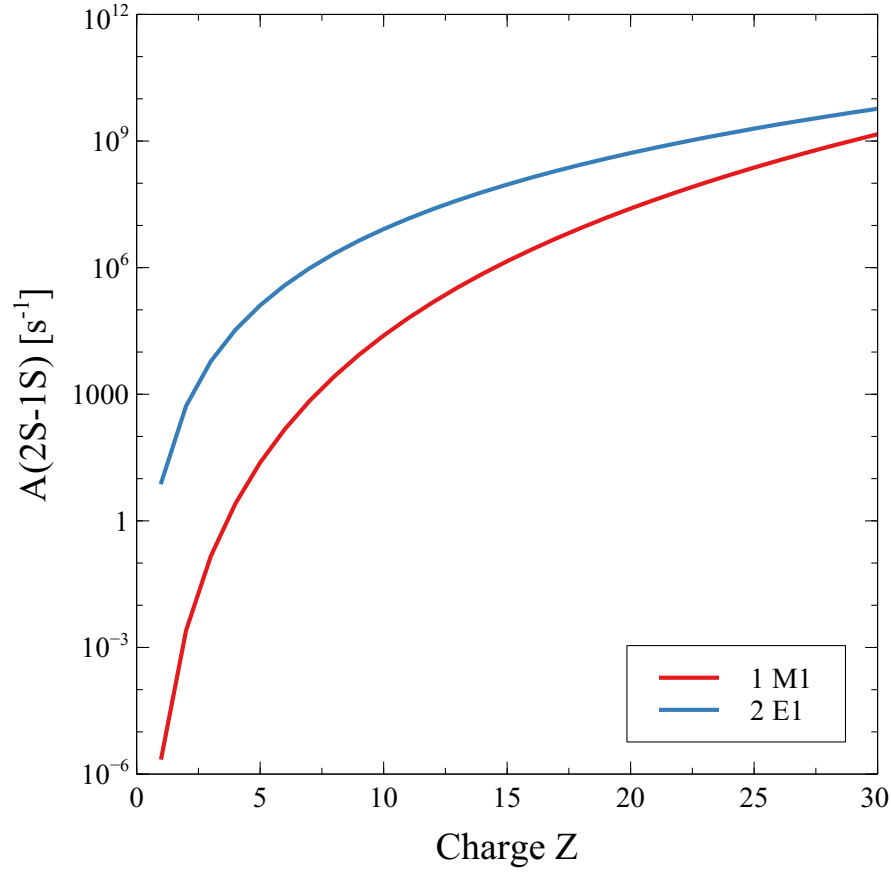


Figure 11. Change in the transition rate due to one and two photon processes. At low- Z , two-photon emission is ~ 7 dex faster than the $M1$ transition while the two are comparable for Fe-peak elements.

Single-photon electric dipole transitions would violate the parity selection rule, but two-photon electric dipole transitions can occur. This produces a broad continuum that, in terms of photon number, peaks at half the energy of $\text{Ly}\alpha$,

Section 11.2.1 of Sobelman (1979) discusses the $2s_{1/2} \rightarrow 1s_{1/2}$ transition in detail (Goldman & Drake 1981).

$$2E1 : A(2s \rightarrow 1s) = 8.230 Z^6 \frac{1 + 3.95(\alpha Z)^2 - 2.04(\alpha Z)^4}{1 + 4.60(\alpha Z)^2} [s^{-1}] \quad (\text{B2})$$

Magnetic dipole transitions are also possible between the two states, but are much weaker than the two-photon transitions for low-charge elements. However, the magnetic dipole transitions have a much stronger dependence on Z (Marrus & Mohr 1979):

$$M1 : A(2s \rightarrow 1s) = \frac{\alpha^9 Z^{10} m e^4}{972 h^3} \approx 2.46 \times 10^{-6} Z^{10} [s^{-1}] \quad (\text{B3})$$

We report both the one- and two-photon emission for all Z . Two-photon emission dominates at low Z , and we report that with the species name (i.e., “H 1”) but with a wavelength twice that of $\text{Ly}\alpha$ (since that is where the two-photon continuum peaks). For iron-group elements, the one and two-photon rates are comparable but do not present a spectroscopic blend since they present line and continuum emission. We report this with the species name with M1 appended (i.e., “H 1 M1”) and the wavelength of the M1 transition, which is very close to the $2p_{1/2} \rightarrow 1s_{1/2}$ transition. We also report a blend (with species label “Blnd”) of sum of the the M1 and $2p_{1/2} \rightarrow 1s_{1/2}$ transitions, and another of the M1, and both $2p \rightarrow 1s$ transitions.

REFERENCES

Alimohamadi, P., & Ferland, G. J. 2022, PASP, 134, 073001,
doi: [10.1088/1538-3873/ac7664](https://doi.org/10.1088/1538-3873/ac7664)

Bahcall, J. N., & Wolf, R. A. 1968, ApJ, 152, 701,
doi: [10.1086/149589](https://doi.org/10.1086/149589)

- Baker, J. G., & Menzel, D. H. 1938, *ApJ*, 88, 52, doi: [10.1086/143959](https://doi.org/10.1086/143959)
- Baker, J. G., Menzel, D. H., & Aller, L. H. 1938, *ApJ*, 88, 422, doi: [10.1086/143997](https://doi.org/10.1086/143997)
- Bauman, R. P., Porter, R. L., Ferland, G. J., & MacAdam, K. B. 2005, *ApJ*, 628, 541, doi: [10.1086/430665](https://doi.org/10.1086/430665)
- Bethe, H. A., & Salpeter, E. E. 1957, *Quantum Mechanics of One- and Two-Electron Atoms* (Springer Science & Business Media, 2013)
- Born, M. 1969, *Modern Physics. Atomic Physics* (London, Blackie, 1969)
- Camilloni, F., Bianchi, S., Amato, R., Ferland, G., & Grinberg, V. 2021, *Research Notes of the American Astronomical Society*, 5, 149, doi: [10.3847/2515-5172/ac0cff](https://doi.org/10.3847/2515-5172/ac0cff)
- Chakraborty, P., Ferland, G. J., Chatzikos, M., et al. 2022, *ApJ*, 935, 70, doi: [10.3847/1538-4357/ac7eb9](https://doi.org/10.3847/1538-4357/ac7eb9)
- Chakraborty, P., Ferland, G. J., Chatzikos, M., Guzmán, F., & Su, Y. 2020a, *ApJ*, 901, 68, doi: [10.3847/1538-4357/abaaab](https://doi.org/10.3847/1538-4357/abaaab)
- . 2020b, *ApJ*, 901, 69, doi: [10.3847/1538-4357/abaaac](https://doi.org/10.3847/1538-4357/abaaac)
- . 2021, *ApJ*, 912, 26, doi: [10.3847/1538-4357/abed4a](https://doi.org/10.3847/1538-4357/abed4a)
- Cota, S. A. 1987, PhD thesis, The Ohio State University
- Dere, K. P., Del Zanna, G., Young, P. R., & Landi, E. 2023, *ApJS*, 268, 52, doi: [10.3847/1538-4365/acec79](https://doi.org/10.3847/1538-4365/acec79)
- Drake, G. W. F. 2006, *Springer Handbook of Atomic, Molecular, and Optical Physics* (Springer Science & Business Media, 2006), doi: [10.1007/978-0-387-26308-3](https://doi.org/10.1007/978-0-387-26308-3)
- Drake, G. W. F., & Swainson, R. A. 1990, *PhRvA*, 41, 1243, doi: [10.1103/PhysRevA.41.1243](https://doi.org/10.1103/PhysRevA.41.1243)
- Elitzur, M. 1992, *Astronomical masers*, Vol. 170 (Springer Dordrecht, 1992), doi: [10.1007/978-94-011-2394-5](https://doi.org/10.1007/978-94-011-2394-5)
- Ferguson, J. W., & Ferland, G. J. 1997, *ApJ*, 479, 363, doi: [10.1086/303880](https://doi.org/10.1086/303880)
- Ferland, G. 1999a, in *Astronomical Society of the Pacific Conference Series*, Vol. 162, *Quasars and Cosmology*, ed. G. Ferland & J. Baldwin, 147
- Ferland, G. J. 1999b, *PASP*, 111, 1524, doi: [10.1086/316466](https://doi.org/10.1086/316466)
- Ferland, G. J., Izotov, Y., Peimbert, A., et al. 2010, in *Proceedings of the International Astronomical Union*, Vol. 268, *Light Elements in the Universe*, ed. C. Charbonnel, M. Tosi, F. Primas, & C. Chiappini, 163–167, doi: [10.1017/S1743921310004011](https://doi.org/10.1017/S1743921310004011)
- Ferland, G. J., Korista, K. T., Verner, D. A., et al. 1998, *PASP*, 110, 761, doi: [10.1086/316190](https://doi.org/10.1086/316190)
- Ferland, G. J., & Persson, S. E. 1989, *ApJ*, 347, 656, doi: [10.1086/168156](https://doi.org/10.1086/168156)
- Ferland, G. J., & Rees, M. J. 1988, *ApJ*, 332, 141, doi: [10.1086/166639](https://doi.org/10.1086/166639)
- Ferland, G. J., Porter, R. L., van Hoof, P. A. M., et al. 2013, *RMxAA*, 49, 137, doi: [10.48550/arXiv.1302.4485](https://doi.org/10.48550/arXiv.1302.4485)
- Ferland, G. J., Chatzikos, M., Guzmán, F., et al. 2017, *RMxAA*, 53, 385, doi: [10.48550/arXiv.1705.10877](https://doi.org/10.48550/arXiv.1705.10877)
- Goldman, S. P., & Drake, G. W. F. 1981, *PhRvA*, 24, 183, doi: [10.1103/PhysRevA.24.183](https://doi.org/10.1103/PhysRevA.24.183)
- Gunasekera, C. M., Chatzikos, M., & Ferland, G. J. 2022, *Astronomy*, 1, 255, doi: [10.3390/astronomy1030015](https://doi.org/10.3390/astronomy1030015)
- Gunasekera, C. M., van Hoof, P. A. M., Chatzikos, M., & Ferland, G. J. 2023, *Research Notes of the American Astronomical Society*, 7, 246, doi: [10.3847/2515-5172/ad0e75](https://doi.org/10.3847/2515-5172/ad0e75)
- Hjerting, F. 1938, *ApJ*, 88, 508, doi: [10.1086/144000](https://doi.org/10.1086/144000)
- Hubeny, I., & Mihalas, D. 2015, *Theory of Stellar Atmospheres. An Introduction to Astrophysical Non-equilibrium Quantitative Spectroscopic Analysis* (Princeton University Press, 2014)
- Hummer, D. G., & Kunasz, P. B. 1980, *ApJ*, 236, 609, doi: [10.1086/157779](https://doi.org/10.1086/157779)
- Igarashi, A., Ohsaki, A., & Nakazaki, S. 2003, *Journal of the Physical Society of Japan*, 72, 1073, doi: [10.1143/JPSJ.72.1073](https://doi.org/10.1143/JPSJ.72.1073)
- Jackson, J. D. 1998, *Classical Electrodynamics*, 3rd Edition (Wiley-VCH, 1998)
- Jitrik, O., & Bunge, C. F. 2004, *Journal of Physical and Chemical Reference Data*, 33, 1059, doi: [10.1063/1.1796671](https://doi.org/10.1063/1.1796671)
- Kaastra, J. S., & Mewe, R. 1993, *A&AS*, 97, 443
- Kalkofen, W. 1984, *Methods in Radiative Transfer*. (Cambridge University Press, 1984)
- Lykins, M. L., Ferland, G. J., Kisielius, R., et al. 2015, *ApJ*, 807, 118, doi: [10.1088/0004-637X/807/2/118](https://doi.org/10.1088/0004-637X/807/2/118)
- Mao, J., Del Zanna, G., Gu, L., Zhang, C. Y., & Badnell, N. R. 2022, *ApJS*, 263, 35, doi: [10.3847/1538-4365/ac9c57](https://doi.org/10.3847/1538-4365/ac9c57)
- Marrus, R., & Mohr, P. J. 1979, *Advances in Atomic and Molecular Physics*, 14, 181, doi: [10.1016/S0065-2199\(08\)60128-1](https://doi.org/10.1016/S0065-2199(08)60128-1)
- Netzer, H., Elitzur, M., & Ferland, G. J. 1985, *ApJ*, 299, 752, doi: [10.1086/163741](https://doi.org/10.1086/163741)
- Osterbrock, D. E., & Ferland, G. J. 2006, *Astrophysics of gaseous nebulae and active galactic nuclei* (University Science Books, 2006)
- Pengelly, R. M., & Seaton, M. J. 1964, *MNRAS*, 127, 165, doi: [10.1093/mnras/127.2.165](https://doi.org/10.1093/mnras/127.2.165)
- Porter, R. L., Bauman, R. P., Ferland, G. J., & MacAdam, K. B. 2005, *ApJL*, 622, L73, doi: [10.1086/429370](https://doi.org/10.1086/429370)
- Porter, R. L., & Ferland, G. J. 2007, *ApJ*, 664, 586, doi: [10.1086/518882](https://doi.org/10.1086/518882)
- Porter, R. L., Ferland, G. J., & MacAdam, K. B. 2007, *ApJ*, 657, 327, doi: [10.1086/510880](https://doi.org/10.1086/510880)
- Porter, R. L., Ferland, G. J., MacAdam, K. B., & Storey, P. J. 2009, *MNRAS*, 393, L36, doi: [10.1111/j.1745-3933.2008.00593.x](https://doi.org/10.1111/j.1745-3933.2008.00593.x)
- Porter, R. L., Ferland, G. J., Storey, P. J., & Detisch, M. J. 2012, *MNRAS*, 425, L28, doi: [10.1111/j.1745-3933.2012.01300.x](https://doi.org/10.1111/j.1745-3933.2012.01300.x)
- . 2013, *MNRAS*, 433, L89, doi: [10.1093/mnras/lt049](https://doi.org/10.1093/mnras/lt049)
- Rutten, R. J. 2003, *Radiative Transfer in Stellar Atmospheres* (Springer Science & Business Media, 2003)
- Shaw, G., Ferland, G. J., Abel, N. P., Stancil, P. C., & van Hoof, P. A. M. 2005, *ApJ*, 624, 794, doi: [10.1086/429215](https://doi.org/10.1086/429215)

- Sobelman, I. I. 1979, Atomic spectra and radiative transitions (Springer Series in Chemical Physics)
- Walling, R. S., & Weisheit, J. C. 1988, PhR, 162, 1, doi: [10.1016/0370-1573\(88\)90079-8](https://doi.org/10.1016/0370-1573(88)90079-8)
- Wells, R. J. 1999, JQSRT, 62, 29, doi: [10.1016/S0022-4073\(97\)00231-8](https://doi.org/10.1016/S0022-4073(97)00231-8)
- XRISM Science Team. 2020, arXiv e-prints, arXiv:2003.04962, doi: [10.48550/arXiv.2003.04962](https://doi.org/10.48550/arXiv.2003.04962)
- Yerokhin, V. A., & Shabaev, V. M. 2015, Journal of Physical and Chemical Reference Data, 44, 033103, doi: [10.1063/1.4927487](https://doi.org/10.1063/1.4927487)
- Zygelman, B., & Dalgarno, A. 1987, PhRvA, 35, 4085, doi: [10.1103/PhysRevA.35.4085](https://doi.org/10.1103/PhysRevA.35.4085)